

TROPICAL CYCLONE MORPHOLOGY FROM SPACEBORNE SYNTHETIC APERTURE RADAR

BY XIAOFENG LI, JUN A. ZHANG, XIAOFENG YANG, WILLIAM G. PICHEL, MARK DeMARIA, DAVID LONG, AND ZIWEI LI

Sea surface imprints of 83 hurricanes show features such as eye structure, mesovortices, rainbands, and arc clouds, as well as rarities such as high winds within an eye.

Ever since the launch of the first generation of meteorological satellites in the 1960s, Atlantic tropical cyclones and western Pacific counterpart typhoons have been extensively monitored from operational polar-orbiting and geostationary satellite sensors. The striking tropical cyclone cloud pictures taken by these conventional weather satellites have appeared in many journal/magazine covers, newspapers, and television programs. These images are usually acquired by passive remote sensing instruments operating in the visible (Vis) and infrared (IR) bands.

What we view from these images is the cloud-top structure of the tropical cyclones at kilometer spatial resolution. However, the intense air-sea interaction near the ocean surface cannot be directly revealed by these Vis-IR satellite images. With the advance of spaceborne microwave remote sensing, microwave data are also used extensively for tropical cyclone analysis. The advantage of microwave data such as Special Sensor Microwave Imager (SSM/I) and Tropical Rainfall Measuring Mission (TRMM) imagery and Quick Scatterometer (QuikSCAT) and Advanced Scatterometer (ASCAT) scatterometer data is that they can see through most clouds and make operational measurements at the air-sea interface. The spatial resolution of these measurements is usually in the range of kilometers to tens of kilometers. In this study, we analyze a group of high-resolution images acquired by spaceborne synthetic aperture radar (SAR) to obtain even higher resolution. The main advantage of SAR over existing passive microwave imagery and scatterometer data is the high spatial resolution usually ranging from 10 to 100 m.

In 1978, the first spaceborne microwave SAR on board the National Aeronautics and Space Administration (NASA) *Seasat* was launched (e.g., Fu and Holt 1982). Since then, tropical cyclones have also been observed on SAR images. A SAR sensor differs from Vis-IR sensors in that it is an active microwave

AFFILIATIONS: X. LI—GST, NOAA/NESDIS, College Park, Maryland; ZHANG—Hurricane Research Division, AOML, NOAA, Miami, Florida; YANG AND Z. LI—Institute of Remote Sensing Applications, Chinese Academy of Sciences, Beijing, China; PICHEL AND DeMARIA—STAR, NOAA/NESDIS, College Park, Maryland; LONG—Electrical and Computer Engineering Department, Brigham Young University, Provo, Utah

CORRESPONDING AUTHOR: Xiaofeng Yang, No. 20A Datun Rd., Chaoyang District, Beijing 100101, China
E-mail: yangxf@irsa.ac.cn

The abstract for this article can be found in this issue, following the table of contents.

DOI:10.1175/BAMS-D-11-00211.1

In final form 29 April 2012
©2013 American Meteorological Society

radar that emits radar pulses that can penetrate through clouds. SAR then receives the radar backscatter, quantified by the physical value known as the normalized radar cross section (NRCS), from the ocean surface return—a process quite similar to the QuikSCAT scatterometer wind retrieval. As a result, a SAR image shows the sea surface imprint of a tropical cyclone, not a tropical cyclone cloud-top image. For a given radar position, look angle, and direction, NRCS is related to the surface roughness and is affected by sea surface winds (both direction and speed), rain roughening of the surface, waves, and other atmospheric and oceanic processes that modulate the sea surface Bragg wave and surface wave spectra (e.g., Valenzuela 1978). While the imaged NRCS is also affected by attenuation and scattering by rain in the atmosphere (e.g., Nie and Long 2008), the primary signal is from the surface. This allows us to extract information right at the air–sea boundary where the most intense air–sea interaction happens. Compared to conventional Vis–IR sensors, SAR has higher resolution (<100-m spatial resolution). Its swath (450 km for ScanSAR mode images) is usually large enough to cover an entire tropical cyclone. Another advantage is that microwave SAR can image the ocean surface under all weather conditions—day and night. With the increasing number of SAR satellites that have become available since the early 1990s, tropical cyclones are frequently observed in SAR images, such as those obtained from the European Space Agency’s (ESA) Remote Sensing Satellite (*ERS-1/-2*) and *Envisat* satellites and the Canadian Space Agency’s (CSA) *Radarsat-1/-2* satellites, among others. The disadvantages of SAR are its data availability and high cost. As of 2012, there is no governmental operational SAR mission in space. However, operational SAR missions are being planned by both ESA (Sentinel-1) and CSA (Radarsat Constellation Mission), with five satellites scheduled for launch in the coming years. This constellation of operational SAR satellites will, for the first time, provide tropical cyclone researchers and forecasters with the timely access to SAR images necessary to stimulate broader and deeper investigation of tropical cyclones, especially at the air–sea boundary.

In the literature, extracting quantitative tropical cyclone information from SAR images has been a focus of several studies over the past decade. Scientists have tried to use limited SAR images acquired from different SAR missions to understand tropical cyclone eye structure, oceanic swell waves, wind rolls, and tropical cyclone wind speeds. Friedman and Li (2000) characterized the ocean surface response to tropical

cyclone wind and rain from two *Radarsat-1* SAR images covering Hurricane Bonnie (1998). Katsaros et al. (2000) analyzed four *Radarsat-1* SAR hurricane images and discovered the 3–6-km wavelength roll vortices associated with the secondary circulations between the main rainbands of a hurricane. Li et al. (2002) detailed the refraction of hurricane-generated oceanic swell waves at the Gulf Stream north wall. Du and Vachon (2003) developed a wavelet technology to extract hurricane eye information from eight *Radarsat-1* SAR images. Limited case studies by Horstmann et al. (2005) and Shen et al. (2006) showed the capabilities of using single-polarization *Radarsat-1* SAR for high-resolution wind speed mapping with existing geophysical model functions (GMF). Yang et al. (2011) later showed that the wind retrieval accuracy is, however, highly sensitive to the NRCS calibration accuracy. The NRCS errors are from both SAR instrument calibration and from differences in receiving/processing infrastructure (i.e., different satellite ground stations and SAR processors). For high winds over 20 m s^{-1} , in storm or hurricane conditions, the 0.5–1.0-dB SAR calibration errors, which are comparable to the current *Envisat* and *Radarsat-1* SAR instrument NRCS calibration errors, induce very large wind retrieval errors owing to the saturation of the SAR wind GMF. Recent studies (Vachon and Wolfe 2011; Zhang and Perrie 2012; Zhang et al. 2012) showed promising results by using low-noise-floor C-band polarimetric *Radarsat-2* data for better wind estimation at high wind range. Reppucci et al. (2010) developed a tropical cyclone intensity retrieval method and applied it to a Hurricane Katrina (2005) image acquired by the ESA *Envisat* and then used five additional hurricane images to validate the results.

Sporadic case studies from previous research shed light on the potential of using SAR-derived information for tropical cyclone research, but the small number of case studies do not provide a complete view of the sea surface response to tropical cyclone wind forcing. As we analyze more SAR images, we often find inconsistencies from both an image segmentation/classification and a physical retrieval point of view indicating that the results from tropical cyclone case studies cannot be generalized. In this study, 161 *Radarsat-1* SAR tropical cyclone images over a 10-yr span have been investigated. Among these, 73 contain complete tropical cyclone eye structure. We also acquired 10 *Envisat* SAR tropical cyclone images from ESA. In this study, we analyzed the 83 SAR tropical cyclone images to generate the first set of SAR-derived statistics on ocean surface

response to tropical cyclones. The morphology of the tropical cyclone eye in terms of shape and size distribution is presented and discussed within the context of tropical cyclone dynamics. In addition, examples of detailed atmospheric phenomena generated within tropical cyclones—including eye/eyewall, rainband, boundary layer rolls, arc cloud, and mesovortices (Fig. 1)—are presented and discussed.

SAR IMAGERY AND ANCILLARY DATA.

All 73 *Radarsat-1* SAR images used in this study are processed by CSA. The images are georeferenced ScanSAR wide beam (SCW) products with a pixel spacing of 50 m (range) \times 50 m (azimuth). *Radarsat-1* provides horizontal-transmit and horizontal-receive (HH polarization) data. The spatial resolution and swath of a SCW image are 100 m and 500 km, respectively. The images are acquired during Northern Hemisphere summer months (May–October) between 2001 and 2007. Among these, there are 25 typhoons and 38 hurricanes. The 10 *Envisat* SAR images are provided by ESA. One image is acquired in April, and the rest are acquired in August and September between 2004 and 2010. There are five typhoons and five hurricanes. Eight *Envisat* SAR images are wide swath mode (WSM) images with a medium resolution of 150 m and a swath of 405 km at HH or vertical-transmit and vertical-receive (VV) polarization. The other two images are image mode data; one has a spatial resolution of 30 m [image mode precision (IMP)] and the other has a spatial resolution of 150 m [image mode medium (IMM)]. The swath width of both is 100 km.

The storm intensity data are obtained from the North Atlantic Hurricane Database (HURDAT) best-track data for hurricanes and Japan Meteorological Agency Regional Specialized Meteorological Center, Tokyo (RSMC), best-track data for typhoons. The original RSMC wind data is a 10-min averaged measurement (Knapp and Kruk 2010). In this study, the 6-hourly wind product is used. Both best-track datasets are ASCII (text) files containing the 6-hourly (0000, 0600, 1200, and 1800 UTC) center locations (latitude and longitude in tenths of degrees) and intensities (maximum 1-min surface wind speeds in knots and minimum central pressures in millibars) for tropical storms and hurricanes/typhoons. Among the 83

tropical cyclones captured at the SAR imaging time (not the maximum intensity the tropical cyclones reached during their life span), 1 is a tropical depression, 19 are tropical storms, 29 are category 1 hurricanes, 28 are category 2, 1 is category 3, 3 are category 4, and 2 are category 5 storms. This wide range of intensities allows us to investigate how the shape and size of the tropical cyclone eye as observed in the SAR images relate to the intensity of a storm. We list all basic characteristics of these cyclones derived from the SAR images in Table 1.

TROPICAL CYCLONE EYE MORPHOLOGY AND DYNAMICS.

Understanding the asymmetric dynamics of intense vortices such as tropical cyclones is crucial for understanding the physical mechanisms that control vortex evolution and intensity change. During the past decades, asymmetric processes near and within the core of tropical cyclones have been extensively studied in numerical simulations (e.g., Schubert et al. 1999; Nolan and Montgomery 2000; Kossin et al. 2002; Yang et al. 2007; Rozoff et al. 2009). Observational studies (e.g., Reasor et al. 2000; Kossin and Eastin 2001; Kossin and Schubert 2004; Aberson et al. 2006; Reasor et al. 2009) also documented the important role of asymmetric vorticity dynamics in explaining some of the physics of tropical cyclone intensity change. The SAR images listed in this study provide us a new tool for investigating the asymmetric structure of the tropical cyclone eye and/or eyewall.

The sea surface imprint of tropical cyclones as depicted in SAR images have similarities to the depiction of these storms in Vis–IR cloud images but with much higher resolution. However, we remind the reader that the SAR images are of the surface

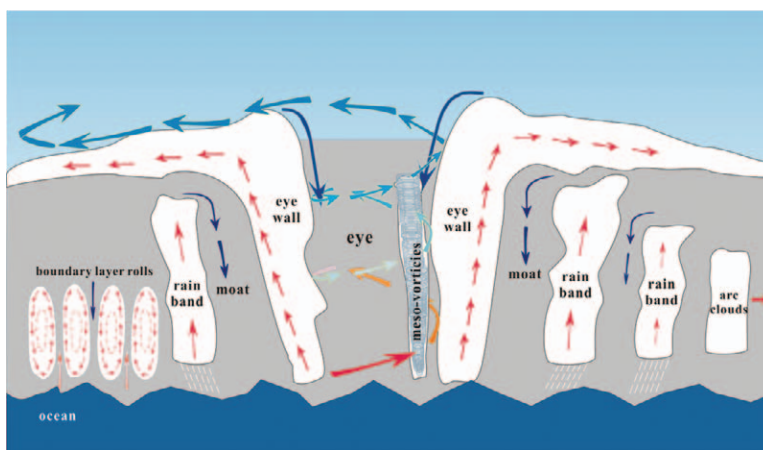


FIG. 1. Schematic plot of tropical cyclone structure and atmospheric phenomena including eye/eyewall, rainband, boundary layer rolls, arc cloud, and mesovortices.

TABLE 1. Basic tropical cyclone information derived from 83 tropical storms observed by SAR. Cyclone locations are eastern Pacific (EPA), western Pacific (WPA), and Atlantic (ATL). SAR types are Radarsat-1 (RI) and Advanced SAR (ASA) (i.e., Envisat). Saffir–Simpson hurricane scales based on wind speed: tropical depression (TD; 0–62 km h⁻¹), tropical storm (TS; 63–117 km h⁻¹), and categories 1 (118–153 km h⁻¹), 2 (154–177 km h⁻¹), 3 (178–209 km h⁻¹), 4 (210–249 km h⁻¹), and 5 (≥250 km h⁻¹).

No.	Year	Month	Day	Time	Name	Cyclone location	Center lat	Center lon	Category	Vmax (knot)	Pressure (hPa)	Shape of eye	Area of eye (km ²)	Wavenumber	Eyewall type	SAR
1	2001	8	29	0143:45	Flossie	EPA	19.8	-115.2	I	75	983	elliptic eye	1,122	2	single	RI
2	2001	9	9	0304:25	Gil	EPA	21.3	-135.3	TD	30	1,006	undefined eye	N/A	N/A	N/A	RI
3	2001	9	11	2219:07	Erin	ATL	37.7	-64.5	I	80	976	rectangular eye	2,973	4	mesovortices	RI
4	2001	9	13	1003:10	Erin	ATL	38.5	-61.0	I	70	980	pentagon eye	7,368	5	single	RI
5	2001	9	17	0807:41	Felix	ATL	35.2	-31.6	I	70	981	asymmetric eye	4,134	N/A	N/A	RI
6	2001	9	26	2141:18	Humberto	ATL	42.0	-56.0	I	80	977	elliptic eye	366	2	single	RI
7	2001	9	27	1321:06	Juliette	EPA	20.9	-110.8	2	90	949	elliptic eye	3,224	2	double	RI
8	2001	10	23	0319:25	Narda	EPA	16.0	-135.7	TS	60	990	undefined eye	756	N/A	N/A	RI
9	2001	11	26	2159:51	Olga	ATL	31.7	-56.2	I	65	977	elliptic eye	840	2	single	RI
10	2001	11	28	0947:55	Olga	ATL	32.4	-56.1	I	75	976	circle eye	970	1	single	RI
11	2002	5	30	0150:35	Alma	EPA	14.1	-115.5	2	93	966	circle eye	494	1	double	RI
12	2002	9	2	1120:35	Edouard	ATL	30.3	-79.9	TS	35	1,007	weak eye	N/A	N/A	N/A	RI
13	2002	9	26	0940:26	Kyle	ATL	28.0	-57.9	I	73	982	rectangular eye	1,570	4	single	RI
14	2002	9	27	2203:02	Kyle	ATL	26.2	-61.1	I	66	985	circle eye	1,105	1	single	RI
15	2002	9	28	2312:10	Lili	ATL	18.8	-75.9	I	45	1,001	triangle eye	212	3	single	RI
16	2002	9	30	1107:06	Lili	ATL	19.5	-79.4	I	60	990	circle eye	416	1	single	RI
17	2002	10	3	2228:55	Kyle	ATL	29.0	-67.9	I	55	994	elliptic eye	1,423	2	single	RI
18	2003	7	13	1203:34	Claudette	ATL	24.8	-92.6	TS	50	998	asymmetry eye	N/A	N/A	N/A	RI
19	2003	8	7	0919:06	Etau	WPA	28.2	129.1	2	82	947	elliptic eye	2,363	2	single	RI
20	2003	8	23	2214:03	Krovanh	WPA	18.4	115.2	TS	55	971	rectangular eye	5,829	4	single	RI
21	2003	9	7	0944:57	Fabian	ATL	39.8	-54.6	2	81	966	rectangular eye	2,385	4	single	RI

22	2003	11	30	2043:42	Lupit	WPA	26.9	137.6	1	80	952	elliptic eye	5,512	2	single	RI
23	2004	9	6	0906:22	Ivan	ATL	10.9	-51.5	4	110	952	circle eye	131	0	concentric	RI
24	2004	9	17	0121:43	Javier	EPA	20.2	-111.3	2	100	960	bright circle eye	228	1	single	RI
25	2004	9	28	0926:55	Meari	WPA	29.4	127.4	1	65	965	elliptic eye	3,138	2	single	RI
26	2004	10	23	2118:39	Nock-Ten	WPA	19.7	126.6	2	85	945	elliptic eye	715	2	single	RI
27	2005	6	6	0903:40	Nesat	WPA	21.4	133.7	2	85	945	circle eye	405	1	closed	RI
28	2005	7	13	2006:29	Haitang	WPA	21.2	145.1	1	68	966	asymmetric eye	N/A	N/A	N/A	RI
29	2005	7	21	1930:21	Nalgae	WPA	-	-	TS	43	988	no eye	N/A	N/A	N/A	RI
30	2005	7	23	2301:05	Franklin	ATL	29.6	-73.7	TS	60	1,001	bright eye	243	1	single	RI
31	2005	7	24	0903:40	Banyan	WPA	23.5	136.3	TS	55	975	not organized eye	N/A	N/A	N/A	RI
32	2005	7	25	2053:54	Banyan	WPA	31.7	137.0	TS	42	975	weak eye	N/A	N/A	N/A	RI
33	2005	7	28	2217:15	Franklin	ATL	36.7	-67.2	TS	53	995	asymmetric eye	3,966	N/A	N/A	RI
34	2005	7	29	2149:10	Franklin	ATL	42.4	-58.8	TS	50	999	weak eye circle	4,966	N/A	single	RI
35	2005	8	4	2211:19	Harvey	ATL	31.7	-61.2	TS	58	993	circle eye	143	0	concentric	RI
36	2005	8	5	0955:08	Matsa	WPA	27.2	122.5	1	71	963	sigma shape	1,630	2	single	RI
37	2005	8	5	2142:29	Harvey	ATL	32.2	-57.2	TS	41	998	elliptic eye	1,896	2	single	RI
38	2005	8	13	0236:09	Sanvu	WPA	18.8	125.6	TS	50	985	circle eye	704	0	single	RI
39	2005	8	22	2038:52	Mawar	WPA	24.6	137.0	1	80	950	elliptic to triangle	668	3	single	RI
40	2005	8	27	1128:41	Katrina	ATL	24.4	-84.6	2	99	942	circle eye	382	0	concentric	RI
41	2005	9	5	2137:58	Maria	ATL	32.2	-56.8	2	93	966	elliptic eye	366	2	closed arc	RI
42	2005	9	7	0923:58	Maria	ATL	35.4	-52.7	1	72	981	weak eye elliptic	N/A	N/A	N/A	RI
43	2005	9	9	2121:42	Nate	ATL	34.3	-52.0	TS	47	988	weak eye	N/A	N/A	N/A	RI
44	2005	9	14	1100:57	Ophelia	ATL	33.4	-77.6	1	74	980	pentagon eye	3,454	5	single	RI
45	2005	9	18	0325:08	Jova	EPA	12.8	-139.3	2	85	973	triangle dark eye	376	3	concentric	RI
46	2005	9	19	1522:26	Jova	EPA	15.3	-142.6	2	102	957	elliptic bright	1,000	2	single	RI
47	2005	9	22	0308:42	Kenneth	EPA	14.6	-134.1	TS	45	1,000	rectangular eye	6,047	4	mesovortices	RI

TABLE I. Continued.

No.	Year	Month	Day	Time	Name	Cyclone location	Center lat	Center lon	Category	Vmax (knot)	Pressure (hPa)	Shape of eye	Area of eye (km ²)	Wavenumber	Eyewall type	SAR
48	2005	9	25	0321:45	Kenneth	EPA	16.0	-139.3	I	65	988	circle eye	192	0	concentric eyewall	RI
49	2005	9	30	1319:18	Otis	EPA	20.9	-110.6	I	65	987	triangle dark eye	1,398	3	single	RI
50	2005	10	2	0138:05	Otis	EPA	21.4	-111.9	I	68	980	circle eye	724	1	single	RI
51	2005	10	3	1330:24	Otis	EPA	24.9	-112.9	TS	28	1,003	undefined eye	N/A	N/A	N/A	RI
52	2005	10	14	0912:13	Kirogi	WPA	22.6	131.4	2	85	940	rectangular eye	956	4	double eyewall	RI
53	2005	10	15	2104:06	Kirogi	WPA	24.1	132.7	2	85	940	rectangular eye	2,560	4	single	RI
54	2006	7	3	2053:52	Ewiniar	WPA	15.0	133.2	2	85	950	circle eye	32	0	concentric	RI
55	2006	7	11	0935:42	Billis	WPA	19.2	128.6	TS	55	987	double eye	N/A	N/A	mesovortices	RI
56	2006	7	12	2129:32	Billis	WPA	22.4	124.4	TS	55	975	weak eye	N/A	N/A	N/A	RI
57	2006	7	15	0236:20	Bud	EPA	19.7	-129.8	TS	32	1,003	weak eye	N/A	N/A	N/A	RI
58	2006	7	24	0312:39	Daniel	EPA	15.2	-138.4	2	89	970	weak eye elliptic	N/A	N/A	N/A	RI
59	2006	8	10	1002:54	Saomai	WPA	26.8	120.2	3	97	945	circle eye	108	1	single	RI
60	2006	9	19	0930:59	Gordon	ATL	24.9	-52.2	2	84	974	elliptic eye	1,264	2	single	RI
61	2006	9	20	2152:31	Helene	ATL	25.9	-57.0	2	73	960	elliptic eye	904	2	single	RI
62	2006	9	21	2017:59	Yagi	WPA	22.9	144.3	2	105	910	circle eye	981	1	single	RI
63	2006	9	23	0910:32	Helene	ATL	36.8	-48.5	1	80	962	elliptic eye	1,913	2	single	RI
64	2006	9	25	0810:03	Helene	ATL	43.9	-32.4	1	63	966	asymmetric eye	N/A	N/A	N/A	RI
65	2006	9	30	2238:38	Xangsane	WPA	16.0	109.0	2	72	965	circle eye	370	1	single	RI
66	2007	7	11	2113:14	Man-Yi	WPA	17.4	124.9	2	95	929	elliptic eye	3,063	2	single	RI
67	2007	7	13	0933:45	Man-Yi	WPA	27.7	127.6	2	79	942	elliptic eye	1,530	2	single	RI
68	2007	8	1	2057:57	Usagi	WPA	29.7	133.2	2	90	945	triangle dark eye	1,632	3	single	RI
69	2007	8	17	0950:33	Dean	ATL	14.3	-61.0	2	86	969	rectangular eye	278	4	concentric	RI
70	2007	8	19	2317:51	Dean	ATL	17.4	-77.6	4	125	936	circle eye	279	1	arc cloud	RI

71	2007	8	31	1942:51	Fitow	WPA	27.8	152.9	1	63	971	rectangular eye	3,936	4	single	RI
72	2007	10	4	2133:56	Krosa	WPA	20.4	125.4	2	98	928	circle eye	1,661	1	single	RI
73	2007	10	20	2025:09	Kajiki	WPA	26.8	142.8	2	92	942	circle eye	90	1	double	RI
74	2004	8	25	0152:41	Aere	WPA	25.5	121.0	1	75	960	elliptic eye	1,568	2	single	ASA
75	2005	8	28	1551:16	Katrina	ATL	26.2	-88.3	5	145	909	circle eye	754	1	single	ASA
76	2005	8	30	0124:39	Talim	WPA	21.4	129.2	2	95	901	small eye	162	1	single	ASA
77	2005	9	11	0146:11	Khanun	WPA	27.5	112.3	1	80	950	circle eye	379	1	single	ASA
78	2005	9	22	0344:32	Rita	ATL	26.1	-87.0	5	150	897	bright circle eye	828	1	single	ASA
79	2008	4	18	0231:50	Neoguri	WPA	18.2	111.3	1	80	965	bright circle eye	502	1	single	ASA
80	2008	9	1	0359:19	Gustav	ATL	27.0	-88.4	2	95	953	circle eye	1,395	1	single	ASA
81	2008	9	13	0423:09	Ike	ATL	28.8	-94.6	2	95	940	circle eye	2,984	1	single	ASA
82	2009	9	14	1422:16	Koppu	WPA	20.8	113.8	1	65	975	comma shape	770	N/A	single	ASA
83	2010	9	2	0244:23	Earl	ATL	31.0	-75.0	4	120	932	comma shape	863	N/A	double	ASA

NRCS while Vis-IR images are optical images of the cloud tops. Figure 2 illustrates a number of cyclone eyes. High winds and rain result in brighter NRCS around the eye, which is darker because of lower winds.

There are different shapes of tropical cyclone eyes as shown in Fig. 2. To quantify if the azimuthal wavenumber of the tropical cyclone eye is related to the intensity, we first determine the azimuthal wavenumber for each SAR image. The wavenumber analysis is both quantitative and subjective, based on the shape of the eye. We define an eye of circular shape with concentric eyewall as wavenumber 0 (Fig. 3a). The circular eye with asymmetric eyewall as determined from the SAR image is regarded as wavenumber 1 (Fig. 3b). The elliptical-shaped eye is defined as wavenumber 2 (Fig. 3c). The triangular-shaped eye is defined as wavenumber 3 (Fig. 3d). The square- or rectangular-shaped eye is defined as wavenumber 4 (Fig. 3e), and an eye shaped like a pentagon is defined as wavenumber 5 (Fig. 3f). The above definition of the low-wavenumber asymmetry is consistent with previous studies (e.g., Reasor et al. 2000; Kossin et al. 2002). It is shown that a majority of data exhibit wavenumber 1 and 2 asymmetries in the eye, suggesting that the nature of the inner-core asymmetry is dominated by these two wavenumbers. The azimuthal wavenumbers of the eye asymmetry are plotted as a function of the storm intensity in Fig. 4a. It appears that there is a tendency for an increase in wavenumber as the tropical cyclone intensity decreases. This relationship suggests that stronger storms tend to be more symmetric in the eye.

While the shape of the tropical cyclone eye is a good indication of dynamics related to asymmetric processes and intensity change, the size of the eye can also be an important factor for intensity change. Previous theoretical and numerical studies have tried to understand why and how the tropical cyclone eye is dynamically and thermodynamically formed and how the eye interacts with the eyewall and the circulation in the outer core region (e.g., Smith 1980; Shapiro and Willoughby 1982; Willoughby 1990). While the size of the eye varies from storm to storm, it is observed that the eye usually contracts during the intensification process. However, the determination of which factors determine the eye size is still an open question. Since the SAR image can detect the structure of a storm through clouds, it provides a good estimate of the size of the eye,

and has the potential to improve the understanding of eye size variability.

In measuring the size of the eye, we first manually select the high NRCS gradient at the tropical cyclone eye boundary and then calculate the low NRCS area in the center of the storm based on its geometric shape. The sizes of the eyes from all the images are calculated and are listed in Table 2. It appears that the size of the eye ranges from hundreds to thousands of square kilometers, with a majority of the values less than 1,000 km². When relating the eye size to the storm intensity, we found that stronger storms tend to have a smaller eye (Fig. 4b). This result is consistent with Kimball and Mulekar (2004), who found that the eye size as measured by aircraft and satellite

data tended to decrease with increasing intensity for storms of category 2 and higher, although for weaker storms the sign of the relationship reversed (weaker systems had smaller eyes). Our finding is also consistent with a recent theoretical study on the effect of the size of the eye on tropical cyclone intensity by Shen (2006). He argued that the potential intensity of a tropical cyclone is sensitive to the size of the storm, in terms of the relative dependence of the surface kinetic energy dissipation and the surface enthalpy flux on the area of the high wind region (i.e., the eyewall). A tropical cyclone with a smaller eye tends to develop into a stronger tropical cyclone because the reduction in eye size leads to the decrease of the area of high wind region, which lowers the kinematic

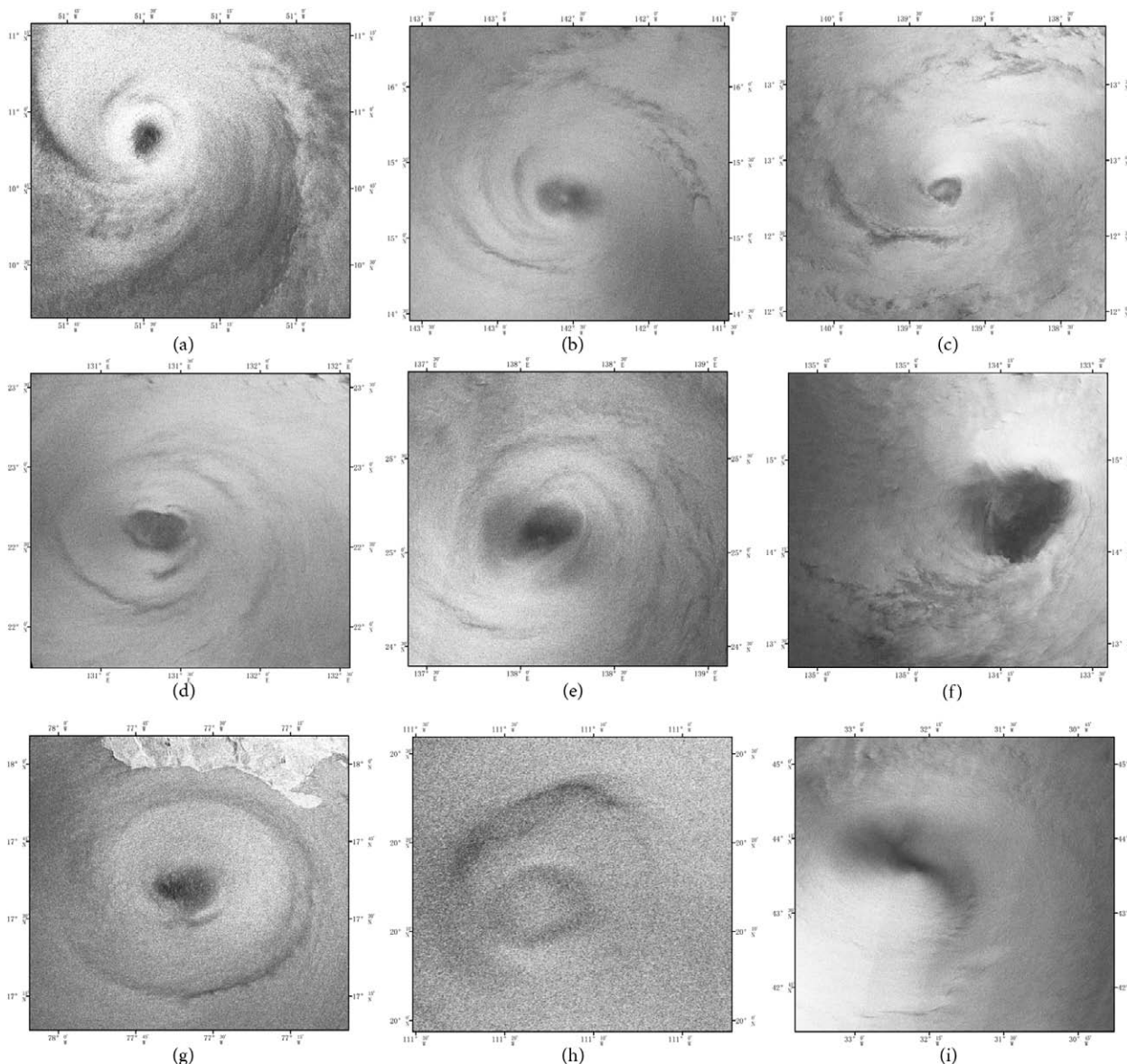


FIG. 2. Examples of SAR hurricanes with different eye shapes.

dissipation to offset the generation of kinetic energy due to surface enthalpy flux.

ATMOSPHERIC AND OCEANIC FEATURES OBSERVED WITHIN TROPICAL CYCLONES.

Mesovortices. Previous observations have shown that intense transient vorticity features are fairly common near the inside edge of eyewalls of numerous intense storms; the example of Tropical Storm (TS) Debby reported by Marks and Houze (1984) is the first known documentation with airborne Doppler data. Mesovortices were also sampled in Hurricane Isabel (Kossin and Schubert 2004; Aberson et al. 2006), and analyzed by Reasor

et al. (2009) in Guillermo. Such vortical features are also clearly evident in several recent high-resolution cloud-representing model simulations (e.g., Braun et al. 2006; Nolan et al. 2009), and moreover in two-dimensional turbulence-resolving models (e.g., Shubert et al. 1999; Kossin and Schubert 2001). The mesovortices are believed to be the result of a combined barotropic–baroclinic instability associated with the annulus of high potential vorticity near and within the eyewall cloud. Montgomery et al. (2006) presented unprecedented observational evidence that high-entropy air inside the low-level eye can sustain the storm at an intensity above that predicted by the potential intensity theory of Emanuel (1986). They articulated that the eye/eyewall mesovortices may be responsible for transferring the high entropy air from the low-level eye to the eyewall. As mentioned before, the use of SAR imagery provides the advantage of observing features through the clouds at very high spatial resolution. The mesovortex features when seen in a SAR image would provide extra evidence that such features do exist at low levels below the clouds. Although mesovortices were found in well-organized cyclones, we also find they exist in much weaker cyclones. Among the 83 images, mesovortices are observed in three weaker cyclones with intensity ranging from tropical storm to category 2 (category 1 Erin, 11 September 2001; category 2 Kenneth, 22 September 2005; Tropical Storm Bilis, 11 July 2006). An example showing mesovortices near the center of Tropical Storm Bilis is shown in Fig. 5. Estimating the surface winds when the mesovortices occur compared to nonvortex cases will be a good research topic for the future.

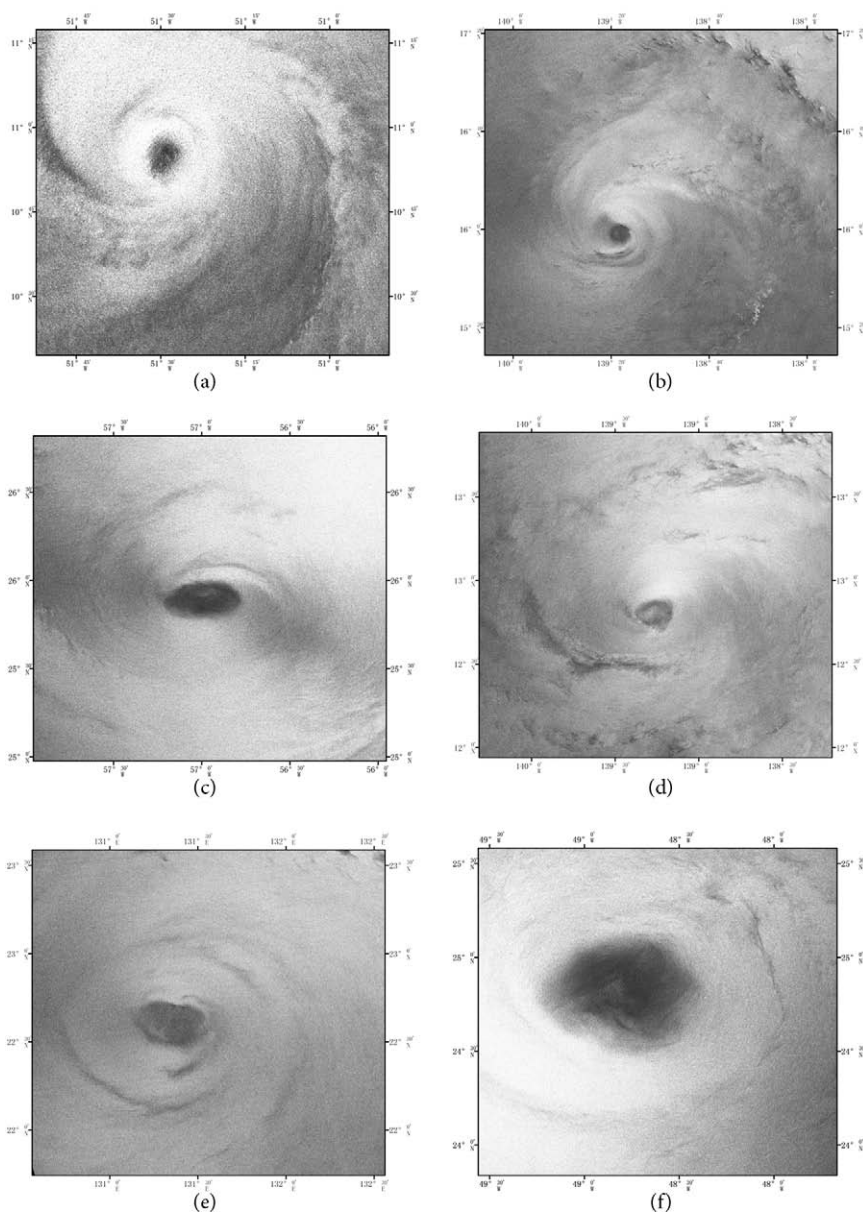


FIG. 3. Examples of SAR hurricanes with different eyewall types.

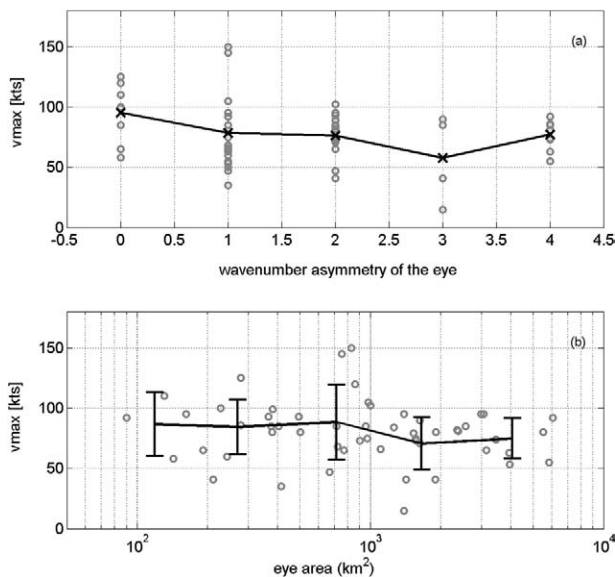


FIG. 4. The wavenumber asymmetry and hurricane eye size versus maximum hurricane wind.

Rainbands and arc clouds. There is a ubiquitous presence of rainband signatures in SAR tropical cyclone images. There are four types of signatures of rainbands apparent in the images: dark (22 August 2005), bright (5 September 2005), dark pattern in the inner rainband and bright pattern in the outer rain (3 July 2006), and half dark and half bright (19 August 2007). Examples are shown in Fig. 6. The bright and dark patterns of rainbands are associated with a combination of five physical mechanisms that change the sea surface roughness (e.g., Bliven and Giovanangeli 1993; Lin et al. 2001). These mechanisms are attenuation due to heavy rain, backscattering from rain drops in the air and ice particles, sea surface capillary waves induced by rain, damping of sea surface waves by rain-induced turbulence, and wind gusts. Different mechanisms will increase or decrease the NRCS measured by a SAR, depending on the observation geometry that varies over the image and the local wind/wave conditions (e.g., Nie and Long 2008). The modulation of C-band NRCS from the first two mechanisms (attenuation and backscattering from rain drops in the air) is small for low rain rates, but

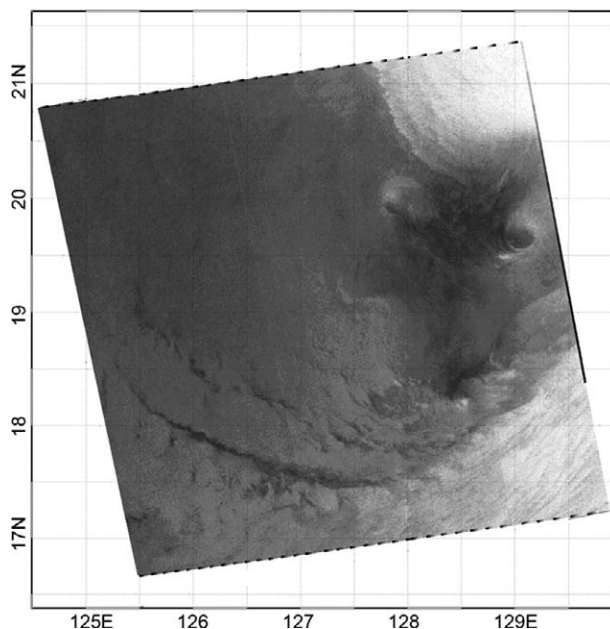


FIG. 5. Hurricane eye/eyewall mesovortices.

can be significant at the high rain rates experienced in hurricanes. These are the primary mechanisms that make rainbands and arc clouds visible in hurricanes (Nie and Long 2007, 2008). However, there is only limited qualitative understanding concerning which mechanisms dominate the NRCS signal in these SAR observations, as the rain rates are unknown. The variations in the rainband signature are thought to be the result of variations in attenuation and backscatter due to spatial variations in rain intensity coupled with the background wind-induced NRCS.

Arc clouds are common features in midlatitude thunderstorms and mesoscale convective systems (MCSs), although they have only occasionally been noted in tropical cyclone (TC) environments in the past (e.g., Knaff and Weaver 2000). It was not until recently that arc clouds have been reported to consistently form in the tropics in the periphery of these tropical disturbances and tropical cyclones, having been noticed in visible satellite images (e.g., Dunion et al. 2010). The observed arc clouds have a length on the order of several hundred kilometers and a life span of several hours. Dunion et al. (2010)

TABLE 2. The number of SAR observations showing different tropical cyclone eye shapes

Wavenumber	0	1	2	3	4	5
Number of SAR images	5	20	20	5	9	2
Max eye area (km ²)	382	2,984	3,138	1,632	6,047	5,610
Mean eye area (km ²)	176	743	1,604	857	2,945	4,531
Min eye area (km ²)	32	90	366	212	956	3,452

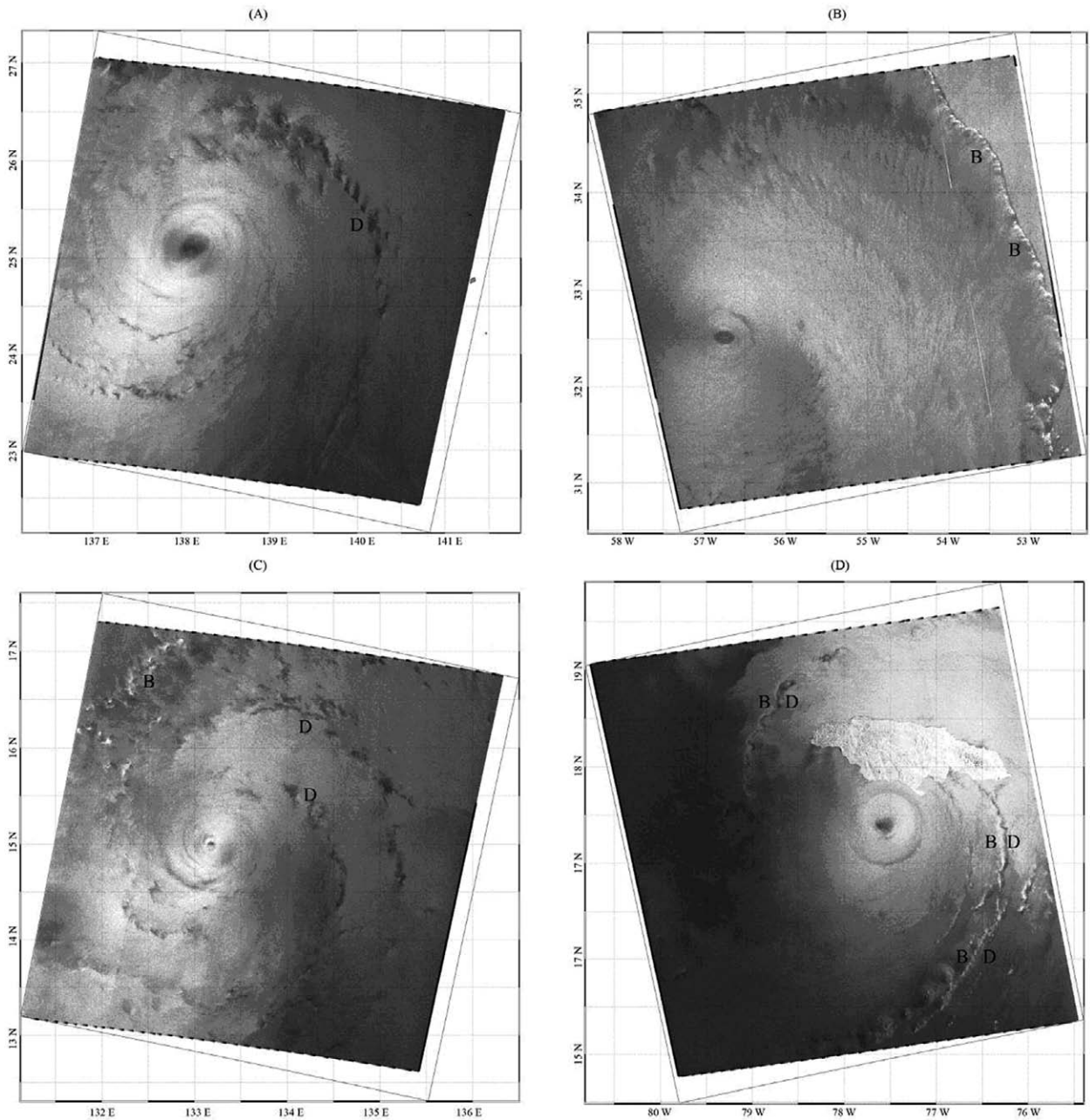


FIG. 6. Different rainband patterns observed in SAR images.

suggested that arc clouds denote the presence of a density current that forms when dry middle-level (~600–800 hPa) air has interacted with precipitation. The convectively driven downdrafts in the vicinity of arc clouds can reach the surface/near surface. These downdrafts can bring cool and dry air to the boundary layer that helps stabilize the boundary layer and inhibits convection. It is hypothesized by Dunion et al. (2010) that the processes leading to the formation of arc cloud events can significantly impact an African easterly wave (AEW) or tropical cyclone—in particular, the relatively smaller and less developed

systems. Among the 83 SAR images, we saw evidence of arc cloud features in two images (Typhoon Guchol and Hurricane Dean, shown in Figs. 6a and 6d). Arc clouds are visible in the SAR NRCS images because of rain effects, both at the surface and in the atmosphere, with some contribution owing to modulation of the local winds by rain-induced wind downdraft (Nie and Long 2008). Since we can estimate the surface wind speed from the SAR image, we can quantify how the arc clouds affect surface winds using future SAR images, especially multipolarization images, as well as possibly estimate the rain rate. Dunion et al.

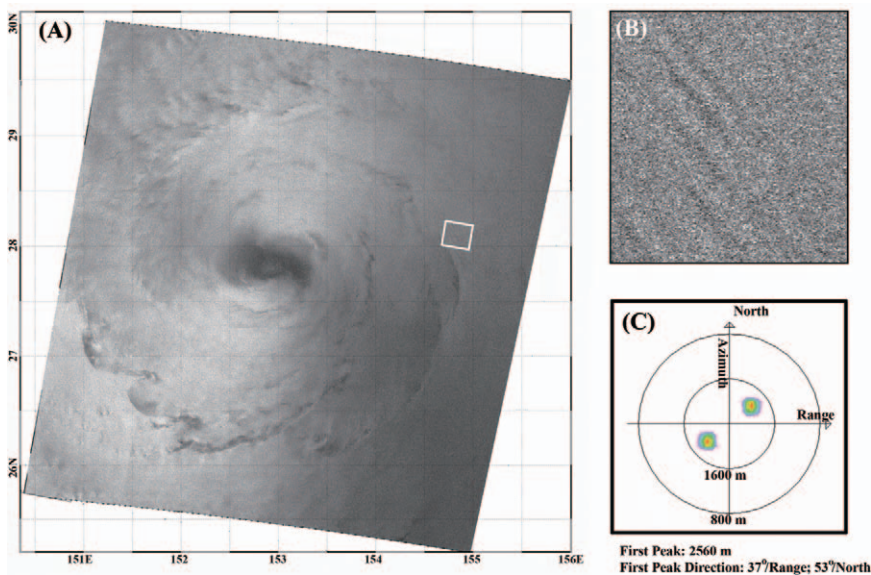


FIG. 7. Analysis of boundary layer rolls within hurricanes.

(2010) proposed that as the arc clouds move away from the convective core region, they tend to create low-level outflow in the quadrant/semicircle of the AEW or TC in which they form, countering the typical low-level inflow that is vital for TC formation and maintenance. Using the SAR images, we can try to test the above hypothesis.

Boundary layer rolls. Boundary layer (BL) rolls or “roll vortices” can have a significant influence on turbulent exchange of momentum, sensible heat, and moisture in the tropical cyclone BL, which is essential for hurricane maintenance and intensification (Zhang et al. 2008). Foster (2005) has developed a theory for roll vortices in curved flow at high wind speeds, such as in hurricanes, suggesting that tropical cyclone BL rolls transport high-momentum air from the upper tropical cyclone BL downward (and low-momentum air from the lower tropical cyclone BL upward) and enhance the transport of air–sea flux. Most previous observational studies on rolls in the tropical cyclone BL to date have focused on land-falling storms (e.g., Wurman and Winslow 1998; Morrison et al. 2005). At this point it remains unclear how frequently BL rolls occur in hurricanes, especially in open-ocean conditions. It is unclear too how tropical cyclone BL rolls modulate the mean and turbulence structure.

SAR can provide useful information for identifying tropical cyclone BL rolls, because streak patterns in sea surface roughness can be explained by change in surface wind speed due to the formation of BL rolls (e.g., Alpers and Brümmer 1994; Foster 2005; Zhang et al. 2008). There are a number of SAR hur-

ricane images that contain roll information in our database. An example is given in Fig. 7a. We extract a full-resolution subimage (Fig. 7b) and perform a fast Fourier transform (FFT) analysis (Fig. 7c) to show the spatial dimension (2–3 km) and orientation direction of the BL rolls within the hurricane. The BL rolls are found to be generally in line with the wind direction. These BL rolls are also related to boundary layer height, as they can be regarded as large eddies expanding the whole boundary layer.

With the extensive dataset of SAR images summarized in this work, quantifying the frequency of occurrence, location relative to the storm center, and wavelength distribution of the tropical cyclone BL rolls becomes possible. Since more and more research aircraft missions are being conducted in both Atlantic and Pacific tropical cyclones, the chance to obtain SAR images coincident with aircraft observations is larger than before. Our future research activities will include searching for collocated SAR images and aircraft data collected by the National Oceanic and Atmospheric Administration (NOAA), Air Force, and other agencies to investigate the influence of rolls on the mean and turbulence structure in hurricanes, following the methodology described by Zhang et al. (2008). It is believed that the effects of tropical cyclone BL rolls can be better understood and eventually parameterized with success in hurricane models through analyzing the concurrent flight-level, dropsonde, Doppler radar data and SAR images.

Storm patterns on land. Most of the tropical cyclone SAR images show conventional storm patterns over the ocean. However, there are a few SAR images that have revealed several interesting phenomena that are not well understood.

The first example is that two of the SAR images show that the storm systems partially cover the land surface (Fig. 8). The 7 August 2003 (Fig. 8a) image shows category 3 Typhoon Etau over Kakeroma Island, Japan. One can clearly see the single eyewall as a bright circular pattern in the image. This eyewall shows a brighter pattern both over ocean and land (between

the two “D”s in Fig. 8a). The dark patterns (marked as D in Fig. 8a) in the image also continue from ocean to the land. In addition, the low backscatter area shows a very well-defined typhoon eye over land.

Another example is shown in the 10 August 2006 category 5 Typhoon Saomai image covering the Fujian–Zhejiang coast of China (Fig. 8b). The high spiral tropical cyclone wind pattern is visible over ocean. This storm pattern is continuous across the ocean–land boundary and remains the same structure over land. We believe that these NRCS signatures are due to radar scattering and signal attenuation from intense rain in the atmosphere, which is similar over land and ocean. With appropriate validation, the rain source for the signature can be tested since the NRCS signature will be horizontally displaced by the vertical height of the scattering and attenuation (Nie and Long 2008). This will be a future project.

High wind observed within certain tropical cyclone eyes. Within tropical cyclone eyes, the wind speed is usually low, according to tropical cyclone dynamics (Smith 1980). In general, lower NRCS corresponds to lower sea surface roughness and, thus, lower wind. Seventy nine out of the 83 SAR images in this study demonstrate low NRCS calm areas within tropical cyclone eyes. However, four images show abnormally higher NRCS within the eyes of these tropical cyclones (Fig. 9) than that of surrounding areas, indicating higher roughness regions within some tropical cyclone eyes. At the SAR imaging times of these four storms, the intensity varies from TS to categories 1, 2, and 5. Bright eyes appear on both *Envisat* and *Radarsat-1* images. These may be due to rainfall within the eye, anomalously large wave–swell interaction, or abnormally high winds within the eye.

CONCLUSIONS. Utilization of SAR imagery is a relatively new tool for tropical cyclone research and forecasting because of its limited coverage, lack of operational analysis tools, and high cost. All these impediments are in the process of being swept away. NOAA is implementing an operational SAR wind processing system. ESA and CSA will launch the Sentinel-1 and Radarsat Constellation Mission SAR missions in 2013–16. These missions will be operational and data will be free and open. It is important now to develop new capabilities to use SAR data for tropical cyclone research, as it shows detailed dynamical processes within the tropical cyclone system.

This study demonstrates the advantage of SAR sensors for the imaging of finescale storm patterns

on the sea surface beneath the storm clouds. We are able to view the actual ocean surface responses to the storm-forced winds. Different storm eye shapes are categorized and we find that stronger storms tend to be more symmetric in the eye shape. Examples of eye/eyewall mesovortices are clearly presented because SAR has high spatial resolution (<100 m). Rainbands and arc clouds are all shown and discussed qualitatively. Quantitative studies will be carried out in the future together with measurements from airplane and in situ instruments.

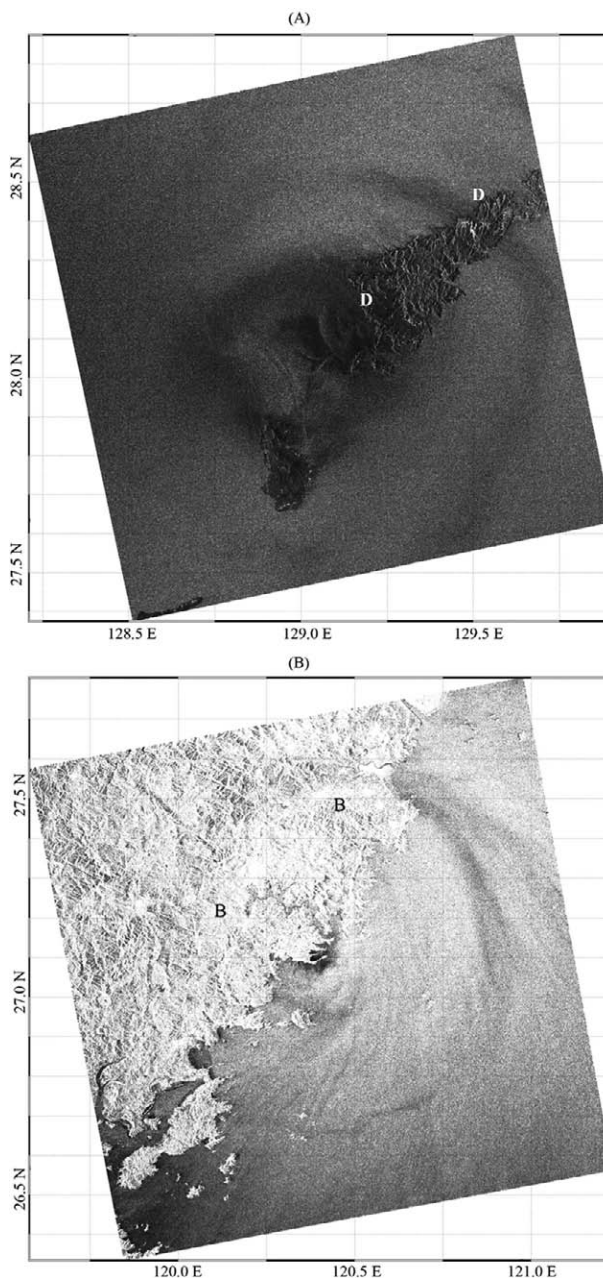


FIG. 8. Hurricane patterns over ocean and land observed on SAR images.

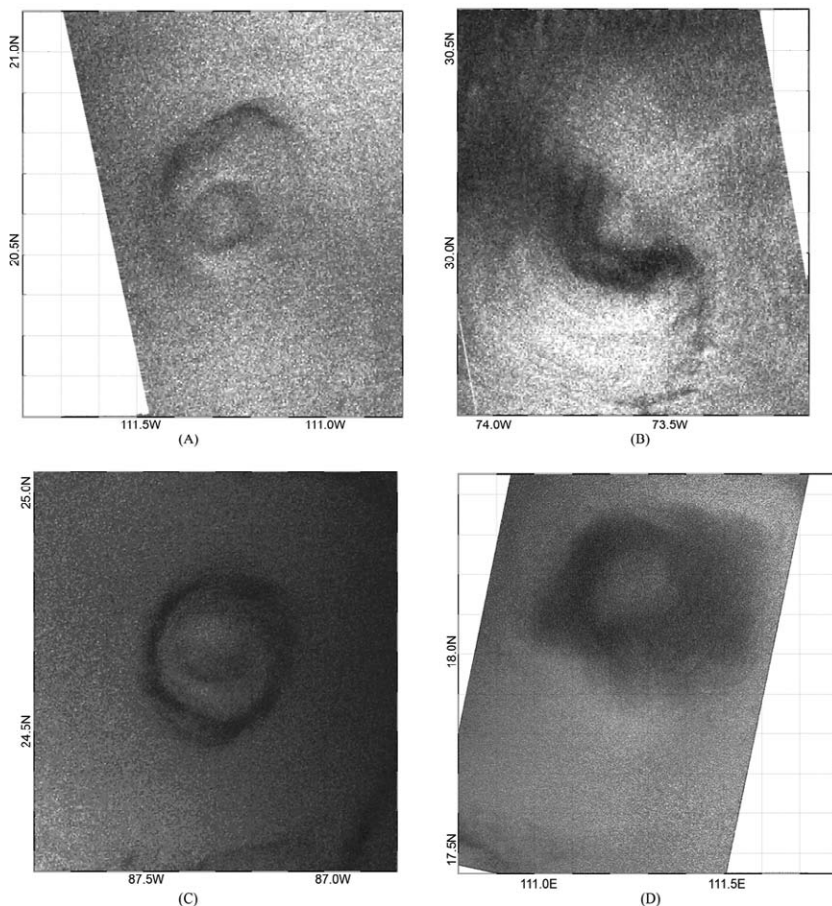


FIG. 9. SAR images showing abnormally high roughness area within hurricane eyes.

SAR images show a few unusual observations. One is that the storm pattern continues across the land–sea boundary. We conjecture that this is due to rain scattering and attenuation in the atmosphere. The other one is that higher NRCS values are observed within some storm eyes, which is usually believed to be a relatively calm area within the storm system. Possible explanations are rain, waves, and abnormally high wind. However, these phenomena cannot be addressed by SAR observation alone. With the increasing number of spaceborne SAR satellites in the next 2–3 years, we believe there will be more simultaneous observations of storm systems from different spaceborne, airborne, and in situ sensors to help researchers understand these phenomena.

ACKNOWLEDGMENTS. *Radarsat-1* SAR images were provided by CSA through the project “Innovative Research and Development of Applications in Using *Radarsat-1* Hurricane SAR Data.” The *Envisat* ASAR images were provided by the European Space Agency under *Envisat* Projects 141 and 6133. The HURDAT best-

track data are obtained from the NOAA National Hurricane Center (www.nhc.noaa.gov/pastall.shtml#hurdat). The RSMC best-track data are obtained from the Japan Meteorological Agency (www.jma.go.jp/jma/jma-eng/jma-center/rsmc-hp-pub-eg/besttrack.html).

This work is also supported in part by National Natural Science Foundation of China under Grants 41228007 and 41201350. The views, opinions, and findings contained in this report are those of the authors and should not be construed as an official NOAA or U.S. government position, policy, or decision.

REFERENCES

- Aberson, S., M. T. Montgomery, M. M. Bell, and M. Black, 2006: Hurricane Isabel (2003): New insights into the physics of intense storms. Part II. Extreme localized wind. *Bull. Amer. Meteor. Soc.*, **87**, 1335–1347.
- Alpers, W., and B. Brümmer, 1994: Atmospheric boundary layer rolls observed by the synthetic aperture radar aboard the ERS-1 satellite. *J. Geophys. Res.*, **99** (C6), 12 613–12 621.
- Bliven, L. F., and J. Giovanangeli, 1993: An experimental study of microwave scattering from rain- and wind-roughened seas. *Int. J. Remote Sens.*, **14**, 855–869.
- Braun, S. A., M. T. Montgomery, and Z. Pu, 2006: High-resolution simulation of Hurricane Bonnie (1998). Part I: The organization of eyewall vertical motion. *J. Atmos. Sci.*, **63**, 19–42.
- Du, Y., and P. W. Vachon, 2003: Characterization of hurricane eyes in RADARSAT-1 images with wavelet analysis. *Can. J. Remote Sens.*, **29**, 491–498.
- Dunion, J., M. D. Eastin, D. S. Nolan, J. Hawkins, and C. Velden, 2010: Arc clouds in the tropical cyclone environment: Implications for TC intensity change. Preprints, *29th Conf. on Hurricanes and Tropical Meteorology*, Tucson, AZ, Amer. Meteor. Soc., 6C.7. [Available online at https://ams.confex.com/ams/29Hurricanes/techprogram/paper_168620.htm.]

- Emanuel, K. A., 1986: An air–sea interaction theory for tropical cyclones. I: Steady-state maintenance. *J. Atmos. Sci.*, **43**, 585–604.
- Foster, R. C., 2005: Why rolls are prevalent in the hurricane boundary layer. *J. Atmos. Sci.*, **62**, 2647–2661.
- Friedman, K. S., and X. Li, 2000: Monitoring hurricanes over the ocean with wide swath SAR. *Johns Hopkins APL Technical Digest*, Vol. 21, No. 1, Applied Physics Laboratory, Laurel, MD, 80–85. [Available online at www.jhuapl.edu/techdigest/TD/td2101/fried.pdf.]
- Fu, L.-L., and B. Holt, 1982: Seasat views oceans and sea ice with synthetic aperture radar. JPL Publ. 81–120, 200 pp.
- Horstmann, J., D. Thompson, F. Monaldo, S. Iris, and H. C. Graber, 2005: Can synthetic aperture radars be used to estimate hurricane force winds? *Geophys. Res. Lett.*, **32**, L22801, doi:10.1029/2005GL023992.
- Katsaros, K., P. W. Vachon, P. G. Black, P. P. Dodge, and E. W. Uhlhorn, 2000: Wind fields from SAR: Could they improve our understanding of storm dynamics? *Johns Hopkins APL Technical Digest*, Vol. 21, No. 1, Applied Physics Laboratory, Laurel, MD, 86–93. [Available online at www.jhuapl.edu/techdigest/TD/td2101/katsaros.pdf.]
- Kimball, S. K., and M. S. Mulekar, 2004: A 15-year climatology of North Atlantic tropical cyclones. Part I: Size parameters. *J. Climate*, **17**, 3555–3575.
- Knaff, J. A., and J. F. Weaver, 2000: A mesoscale low-level thunderstorm outflow boundary associated with Hurricane Luis. *Mon. Wea. Rev.*, **128**, 3352–3355.
- Knapp, K. R., and M. C. Kruk, 2010: Quantifying interagency differences in tropical cyclone best-track wind speed estimates. *Mon. Wea. Rev.*, **138**, 1459–1473.
- Kossin, J. P., and M. D. Eastin, 2001: Two distinct regimes in the kinematic and thermodynamic structure of the hurricane eye and eyewall. *J. Atmos. Sci.*, **58**, 1079–1090.
- , and W. H. Schubert, 2001: Mesovortices, polygonal flow patterns, and rapid pressure falls in hurricane-like vortices. *J. Atmos. Sci.*, **58**, 2196–2209.
- , and —, 2004: Mesovortices in Hurricane Isabel (2003). *Bull. Amer. Meteor. Soc.*, **85**, 151–153.
- , B. D. McNoldy, and W. H. Schubert, 2002: Vortical swirls in hurricane eye clouds. *Mon. Wea. Rev.*, **130**, 3144–3149.
- Li, X., W. Pichel, M. He, S. Wu, K. Friedman, P. Clemente-Colon, and C. Zhao, 2002: Observation of hurricane-generated ocean swell refraction at the Gulf Stream north wall with the RADARSAT-1 synthetic aperture radar. *IEEE Trans. Geosci. Remote Sens.*, **40**, 2131–2142, doi:10.1109/TGRS.2002.802474.
- Lin, I.-I., W. Alpers, V. Khoo, H. Lim, T. K. Lim, and D. Kasilingam, 2001: An ERS-1 synthetic aperture radar image of a tropical squall line compared with weather radar data. *IEEE Trans. Geosci. Remote Sens.*, **39**, 937–945.
- Marks, F. D., Jr., and R. A. Houze Jr., 1984: Airborne Doppler radar observations in Hurricane Debby. *Bull. Amer. Meteor. Soc.*, **65**, 569–582.
- Montgomery, M. T., M. M. Bell, S. Aberson, and M. Black, 2006: Hurricane Isabel (2003): New insights into the physics of intense storms. Part I: Mean vortex structure and maximum intensity estimate. *Bull. Amer. Meteor. Soc.*, **87**, 1335–1347.
- Morrison, I., S. Businger, F. Marks, P. Dodge, and J. A. Businger, 2005: An observational case for the prevalence of roll vortices in the hurricane boundary layer. *J. Atmos. Sci.*, **62**, 2662–2673.
- Nie, C., and D. G. Long, 2007: RADARSAT ScanSAR wind retrieval under hurricane conditions. *Earth Observations Systems XII*, J. Butler and J. Xiong, Eds., International Society for Optical Engineering (SPIE Proceedings, Vol. 6677), 66770K, doi:10.1117/12.732600.
- , and —, 2008: RADARSAT ScanSAR wind retrieval and rain effects on ScanSAR measurements under hurricane conditions. *Proc. IGARSS 2008 Geoscience and Remote Sensing Symp.*, Boston, MA, IEEE International, 493–496.
- Nolan, D. S., and M. T. Montgomery, 2000: The algebraic growth of wavenumber-1 disturbances in hurricane-like vortices. *J. Atmos. Sci.*, **57**, 3514–3538.
- , J. A. Zhang, and D. P. Stern, 2009: Evaluation of planetary boundary layer parameterizations in tropical cyclones by comparison of in-situ data and high-resolution simulations of Hurricane Isabel (2003). Part I: Initialization, maximum winds, and outer core boundary layer structure. *Mon. Wea. Rev.*, **137**, 3651–3674.
- Reasor, P. D., M. T. Montgomery, F. D. Marks Jr., and J. F. Gamache, 2000: Low-wavenumber structure and evolution of the hurricane inner core observed by airborne dual-Doppler radar. *Mon. Wea. Rev.*, **128**, 1653–1680.
- , M. Eastin, and J. F. Gamache, 2009: Rapidly intensifying Hurricane Guillermo (1997). Part I: Low-wavenumber structure and evolution. *Mon. Wea. Rev.*, **137**, 603–631.
- Reppucci, A., S. Lehner, J. Schulz-Stellenfleh, and S. Brusch, 2010: Tropical cyclone intensity estimated from wide-swath SAR images. *IEEE Trans. Geosci. Remote Sens.*, **48**, 1639–1649, doi:10.1109/TGRS.2009.2037143.
- Rozoff, C. M., J. P. Kossin, W. H. Schubert, and P. J. Mulero, 2009: Internal control of hurricane intensity variability: The dual nature of potential vorticity mixing. *J. Atmos. Sci.*, **66**, 133–147.

- Schubert, W. H., M. T. Montgomery, R. K. Taft, T. A. Guinn, S. R. Fulton, J. P. Kossin, and J. P. Edwards, 1999: Polygonal eyewalls, asymmetric eye contraction, and potential vorticity mixing in hurricanes. *J. Atmos. Sci.*, **56**, 1197–1223.
- Shapiro, L. J., and H. E. Willoughby, 1982: The response of balanced hurricanes to local sources of heat and momentum. *J. Atmos. Sci.*, **39**, 378–394.
- Shen, H., W. Perrie, and Y. He, 2006: A new hurricane wind retrieval algorithm for SAR images. *Geophys. Res. Lett.*, **33**, L21812, doi:10.1029/2006GL027087.
- Shen, W., 2006: Does the size of hurricane eye matter with its intensity? *Geophys. Res. Lett.*, **33**, L18813, doi:10.1029/2006GL027313.
- Smith, R. K., 1980: Tropical cyclone eye dynamics. *J. Atmos. Sci.*, **37**, 1227–1232.
- Vachon, P. W., and J. Wolfe, 2011: C-band cross-polarization wind speed retrieval. *IEEE Trans. Geosci. Remote Sens. Lett.*, **8**, 456–459.
- Valenzuela, R. G., 1978: Theories for the interaction of electromagnetic and ocean waves—A review. *Bound.-Layer Meteor.*, **13**, 61–85, doi:10.1007/BF00913863.
- Willoughby, H. E., 1990: Temporal changes of the primary circulation in tropical cyclones. *J. Atmos. Sci.*, **47**, 242–264.
- Wurman, J., and J. Winslow, 1998: Intense sub-kilometer boundary layer rolls in Hurricane Fran. *Science*, **280**, 555–557.
- Yang, B., Y. Wang, and B. Wang, 2007: The effect of internally generated inner-core asymmetries on tropical cyclone potential intensity. *J. Atmos. Sci.*, **64**, 1165–1188.
- Yang, X., X. Li, W. G. Pichel, and Z. Li, 2011: Comparison of ocean surface winds from ENVISAT ASAR, MetOp ASCAT scatterometer, buoy measurements, and NOGAPS model. *IEEE Trans. Geosci. Remote Sens.*, **49**, 4743–4750, doi:10.1109/TGRS.2011.2159802.
- Zhang, B., and W. Perrie, 2012: Cross-polarized synthetic aperture radar: A potential measurement technique for hurricanes. *Bull. Amer. Meteor. Soc.*, **93**, 531–541.
- , —, P. W. Vachon, X. Li, and W. G. Pichel, 2012: Ocean vector winds retrieval from C-band fully polarimetric SAR measurements. *IEEE Trans. Geosci. Remote Sens.*, **50**, 4252–4261, doi:10.1109/TGRS.2012.2194157.
- Zhang, J. A., K. B. Katsaros, P. G. Black, S. Lehner, J. R. French, and W. M. Drennan, 2008: Effects of roll vortices on turbulent fluxes in the hurricane boundary layer. *Bound.-Layer Meteor.*, **128**, 173–189.